Macromolecules

pubs.acs.org/Macromolecules Article

Tunable Sizes and Aspect Ratios of Uniform Hexagonal/Rhombic Nanosheets with a Polyethylene Core via Crystallization-Driven Self-Assembly

Jiali Wu, Boyang Shi, Ding Shen, Hanyu Lv, and Guowei Wang*

Cite This: https://doi.org/10.1021/acs.macromol.5c03517 Read Online

ACCESS | Metrics & More | Article Recommendations | Supporting Information

ABSTRACT: Block copolymers (BCPs) are well-documented to undergo self-assembly into diverse nanostructures. Uniquely, BCPs with crystallizable core-forming blocks undergo crystallization-driven self-assembly (CDSA), typically yielding one-dimensional (1D) nanowires and two-dimensional (2D) nanosheets. However, the precise control over morphologies, sizes, and aspect ratios of 2D nanosheets remains challenging. Herein, we present a one-pot "heating−cooling−aging" CDSA strategy for polyethylene-*block*-poly(4-*tert*-butoxystyrene) (PE-*b*-P*t*BOS) BCPs, which is implemented in a selective solvent of toluene over a broad concentration range of 0.025∼5.0 wt %. This strategy enables the fabrication of uniform hexagonal/rhombic nanosheets with precisely tunable sizes and aspect ratios by manipulating key parameters of the annealing temperature, the degree of polymerization for P*t*BOS (DP_{PtBOS}), and concentration. Specifically, at lower DP_{PtBOS}, spontaneous nucleation and growth enable the rapid fabrication of molecularly thin, uniform, and tunable nanosheets, whereas at higher DP_{PtBOS}, the formation kinetics of such nanosheets slows down significantly. The nanosheet size is facilely tailorable by adjusting the annealing temperature, as this parameter directly modulates the number of crystal nuclei, while the aspect ratios of these hexagonal/rhombic nanosheets can be readily regulated by varying the concentration or DP_{PtBOS}. Uniquely, a deliberate bidirectional morphological transition between hexagonal and rhombic nanosheets can also be achieved by modulating the DP_{PtBOS}, concentration, and cooling rate. This work provides new insights into how experimental parameters influence the CDSA process and provides an efficient, versatile route for the controlled synthesis of 2D nanosheets.

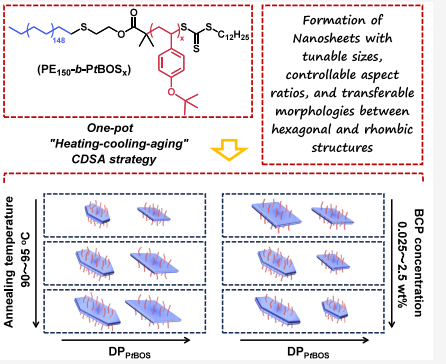

INTRODUCTION

Nanostructures, leveraging their unique structures and functions, have been extensively employed in numerous areas of research and technology, spanning biomedical science, materials science, environmental engineering, etc.[1−7] As the performance of nanostructures is directly impacted by their morphology, size, and composition, the controllable fabrication of these nanostructures has thus become remarkably important. Among all the morphologies, two-dimensional (2D) lamellar micelles exhibit significantly more prominent advantages over zero-dimensional (0D) spherical micelles or one-dimensional (1D) fibrous micelles in extensive fundamental and practical fields owing to their distinct intrinsic characteristics, including a large specific surface area, adjustable aspect ratios (the ratio of length to width), and well-defined morphologies (e.g., hexagons, rectangles, rhombuses).[8−13]

Over the past few decades, self-assembly of amphiphilic block copolymers (BCPs) in solution has evolved into an increasingly adaptable bottom-up strategy, enabling the fabrication of nanostructures with distinct morphologies and tailored functionalities.[14−22] Typically, BCPs with an amorphous core-forming block are capable of forming micelles with spherical, wormlike, or vesicular morphologies, which is generally predictable via packing parameter theory.[17−21] In contrast, BCPs containing crystalline blocks tend to form micelles with low curvature structures such as 1D elongated fibrous micelles and 2D platelet-like micelles through a process known as crystallization-driven self-assembly (CDSA).[16,23−48] Prior reports have documented the CDSA of different BCPs, with crystalline moieties (poly(L-lactide) (PLLA),[23−25] poly(ε-caprolactone) (PCL),[27−30] polyethylene (PE),[36,39−44] poly(3-hexylthiophene) (P3HT),[45,46] polyferrocenyldimethylsilane (PFDMS),[47,48] etc.) acting as the core-forming blocks. Generally, the regulation of micelle sizes can be achieved by adjusting the composition, concentration, and self-assembly conditions of BCPs. Nevertheless, the CDSA-fabricated micelles exhibit a broad size distribution arising from the slower self-nucleation kinetics of molecularly dissolved BCP unimers relative to epitaxial growth. For enhancing the

Received: December 18, 2025
Revised: February 8, 2026
Accepted: February 20, 2026
Published: March 3, 2026

Scheme 1. Synthetic Procedure for PE_{150}-*b*-P*t*BOS$_x$ BCPs and the Corresponding Nanosheets

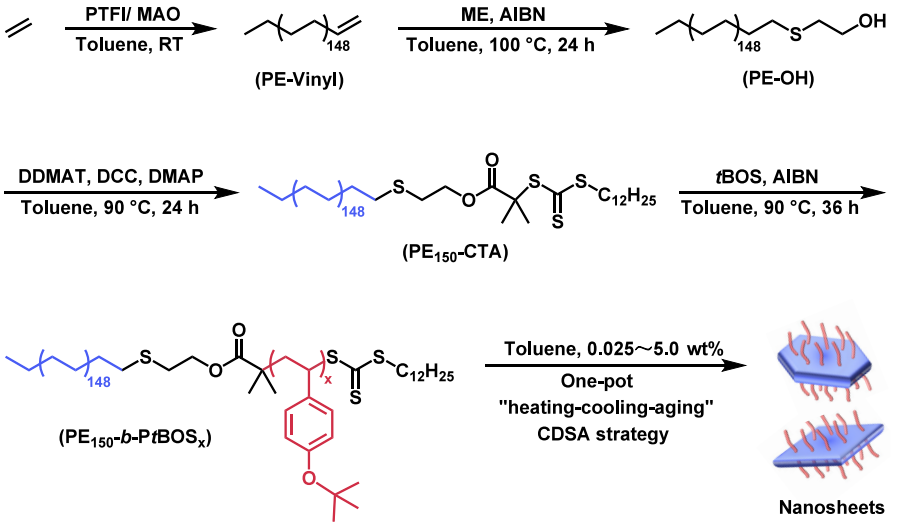

uniformity of assemblies, Manners and Winnik pioneered the "living" CDSA concept—a two-step strategy—for 1D and 2D nanostructures.[49] In their approach, the nucleation and growth processes of crystallites are separated, thereby reducing the polydispersity of the resulting nanostructures. So far, "living" CDSA, including self-seeding and seeded growth approaches, has been demonstrated to exhibit high feasibility for the precise control of nanostructure' sizes and uniformity.[26−30,45−47] Nevertheless, independent control over the length and width of 2D nanosheets remains challenging, as these nanosheets grow simultaneously along both biaxial directions.

Gaining in-depth insight into the intrinsic mechanism of aspect ratio regulation for nanosheets is crucial for realizing precise control over nanosheet sizes and morphologies. This will open up new avenues for the design of nanomaterials with tailored properties, which hold potential applications in various fields including drug delivery, optoelectronics, etc.[29,31−35] Some advances have been made toward these goals. For example, O'Reilly et al. conducted the "living" CDSA of polycaprolactone-*b*-poly(*N*,*N*-dimethylacrylamide) (PCL-*b*-PDMA) and PCL homopolymers.[29] They found that the chain length of PCL exerted a significant influence on the aspect ratios of the resulting nanosheets and attributed this phenomenon to the regulatory effect of crystallization kinetics on the crystallization rates of (110) and (200) crystal planes. Similarly, Manners et al. revealed that the aspect ratios of polycaprolactone-*b*-poly(cobaltocenium amidoethyl methacrylate) (PCL-*b*-PCoAEMA) nanosheets could be jointly regulated by the electrostatic interactions of cationic metal blocks and the crystallization behavior of PCL, leading to differences in the crystallization rates of the platelet crystals along the longitudinal and transverse directions.[32] Furthermore, Choi et al. focused on crystalline polyacetylene containing fluorenes and triisopropylsilyl side chains, successfully realizing independent control over the widths and lengths of 2D nanorectangles by optimizing cosolvents and the CDSA process, providing a new strategy for the precise fabrication of semiconducting 2D nanomaterials.[31] They found that cosolvents enable aspect ratio control by accelerating (010) crystal plane growth compared to that in the (100) plane. Overall, Manners et al. and Choi et al. have made pioneering contributions to this topic, and great progress has been achieved.[29,31,32] Nevertheless, deeper insights into CDSA theory and synergistic control over the sizes, morphologies, and aspect ratios of the 2D nanosheets remain highly desirable, which is expected to facilitate the fabrication of more advanced nanomaterials. Notably, as a general material for industrial applications, crystalline PE is rarely involved in the CDSA process due to the challenging synthesis of PE-based BCPs.[36,39−44]

To address the current limitations of the CDSA process, herein, we constructed a synthetic route for polyethylene-*block*-poly(4-*tert*-butoxystyrene) (PE-*b*-P*t*BOS) through the combination of coordination polymerization and reversible addition−fragmentation chain transfer (RAFT) polymerization, and subsequently evaluated and optimized the CDSA process of PE-*b*-P*t*BOS to achieve systematic control over the geometric parameters of nanosheets in a facile and controllable manner. In detail, the uniform hexagonal/rhombic nanosheets with precisely controllable sizes were prepared using a one-pot "heating−cooling−aging" procedure at concentrations of 0.025∼5.0 wt % (Scheme 1). Factors that influence the sizes, morphologies, and aspect ratios of these nanosheets, mainly comprising the length of the amorphous P*t*BOS segment, annealing temperature, and concentration, were comprehensively investigated. This work represents an alternative efficient route to the fabrication of uniform nanosheets with tunable sizes and aspect ratios via one-pot CDSA process, while also enabling bidirectional morphological transformation of nanosheets between hexagonal and rhombic phases.

RESULTS AND DISCUSSION

Synthesis and Characterization of PE_{150}-*b*-P*t*BOS$_x$ BCPs

The synthetic route of PE_{150}-CTA macroinitiator and PE_{150}-*b*-P*t*BOS$_x$ BCPs with varying degrees of polymerization (DP) of the P*t*BOS block (subscripts 150 and x represent the DP of the PE and P*t*BOS blocks, respectively) are illustrated in Scheme 1. Briefly, the linear vinyl-terminated PE (PE-Vinyl) was first synthesized via the coordination polymerization of ethylene, using bis[*N*-(3-*tert*-butylsalicylidene)cyclopentylaminato]-zirconium(IV) dichloride complex (PTFI) as the catalyst and methylaluminoxane (MAO) as the cocatalyst, and the vinyl termination efficiency was calculated as approximately 85% via ^{1}H NMR spectrum by comparing the integral area of

https://doi.org/10.1021/acs.macromol.5c03517
Macromolecules XXXX, XXX, XXX−XXX

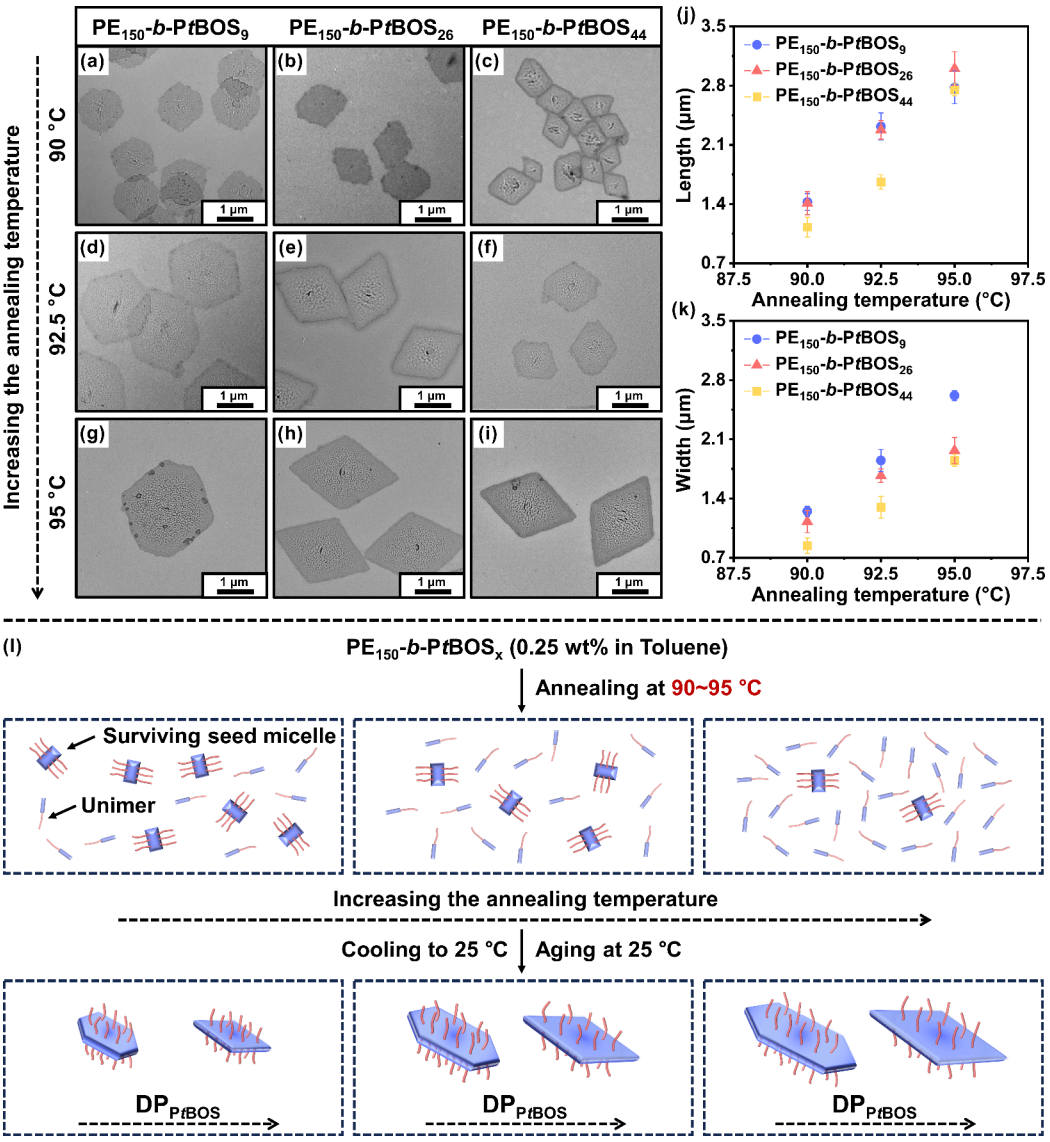

Figure 1. (a–i) Representative TEM images of PE_{150}-*b*-P*t*BOS_x nanosheets obtained via CDSA in toluene at a concentration of 0.25 wt %. All of the samples were annealed at 90, 92.5, and 95 °C for 2.0 h, then naturally cooled to 25 °C in the oil bath, followed by aging at 25 °C for 24.0 h, and finally redispersed by oscillation for sample preparation. (j, k) The numerical distribution of lengths and widths of the PE_{150}-*b*-P*t*BOS_x nanosheets, as statistically obtained from TEM images. (l) Schematic representation of the CDSA process for the PE_{150}-*b*-P*t*BOS_x BCPs.

resonance signals at 0.95 ppm (CH_3-) and 2.10 ppm ($-CH_2CH{=}CH_2$) (Figure S3). Then, the terminal vinyl group on PE-Vinyl was converted to a hydroxyl group, yielding hydroxyl-terminated PE (PE-OH) via the thiol-ene click reaction with excess 2-mercaptoethanol in toluene, using 2,2′-azobis(isobutyronitrile) (AIBN) as the initiator. Subsequently, the macromolecular chain transfer agent PE_{150}-CTA was prepared via an esterification reaction between PE-OH and 2-(dodecylthiocarbonothioylthio)-2-methylpropionic acid (DDMAT) in the presence of *N*,*N*-dicyclohexylcarbodiimide (DCC) and 4-dimethylaminopyridine (DMAP). Notably, the end-group conversion efficiencies for both PE-Vinyl and the subsequent PE-OH were nearly 100%, which was confirmed by the complete disappearance of the resonance signals at 2.10 ppm ($-CH_2CH{=}CH_2$) on PE-Vinyl and 3.75 ppm ($-CH_2OH$) on PE-OH in their ^{1}H NMR spectra (Figure S3). Finally, further RAFT polymerization afforded a series of PE_{150}-*b*-P*t*BOS_x BCPs. The detailed preparation procedure, ^{1}H NMR spectra, and size exclusion chromatography (SEC) characterizations are shown in Scheme 1 and Figures S1–S6.

To confirm that the PE_{150}-*b*-P*t*BOS_x BCPs possess crystallizability to provide the driving force for the subsequent CDSA process, wide-angle X-ray scattering (WAXS) and differential scanning calorimetry (DSC) were employed to examine the crystalline structure and thermal behavior of the PE_{150}-*b*-P*t*BOS_x BCPs. The WAXS analysis revealed that the PE_{150}-CTA precursor and all of the PE_{150}-*b*-P*t*BOS_x BCPs exhibit two distinct crystalline peaks, located at $2\theta = 21.6°$ and 24.0°, corresponding to the (110) and (200) crystalline planes of the PE block, respectively (Figure S7). The intensity of the crystalline peak (110) regularly decreases as the DP_{PtBOS} increases. Meanwhile, PE_{150}-*b*-P*t*BOS_{26} and PE_{150}-*b*-P*t*BOS_{44} exhibit a broad scattering peak at $2\theta = 18.1°$, which corresponds to the amorphous halo of P*t*BOS blocks, with the peak intensity intensifying as DP_{PtBOS} increases. Additionally, the crystallization and melting peaks obtained from DSC analysis further demonstrate that the PE_{150}-CTA homopolymer

https://doi.org/10.1021/acs.macromol.5c03517
Macromolecules XXXX, XXX, XXX−XXX

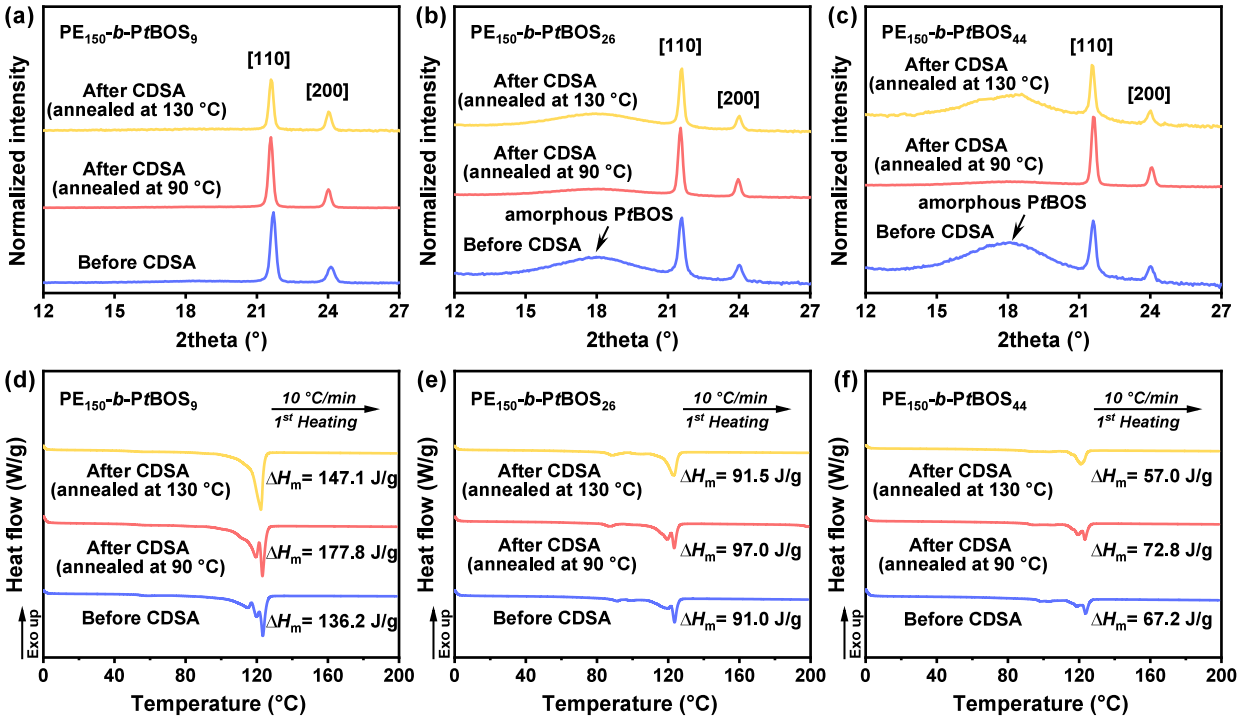

Figure 2. (a–c) WAXS and (d–f) DSC first heating curves of PE_{150}-*b*-P*t*BOS_x (before CDSA) and the corresponding nanosheets obtained via the CDSA process (0.25 wt % in toluene). The PE_{150}-*b*-P*t*BOS_x nanosheets were prepared via annealing at 90 or 130 °C for 2.0 h, then naturally cooled to 25 °C in the oil bath, followed by aging at 25 °C for 24.0 h, and finally subjected to solvent evaporation at room temperature.

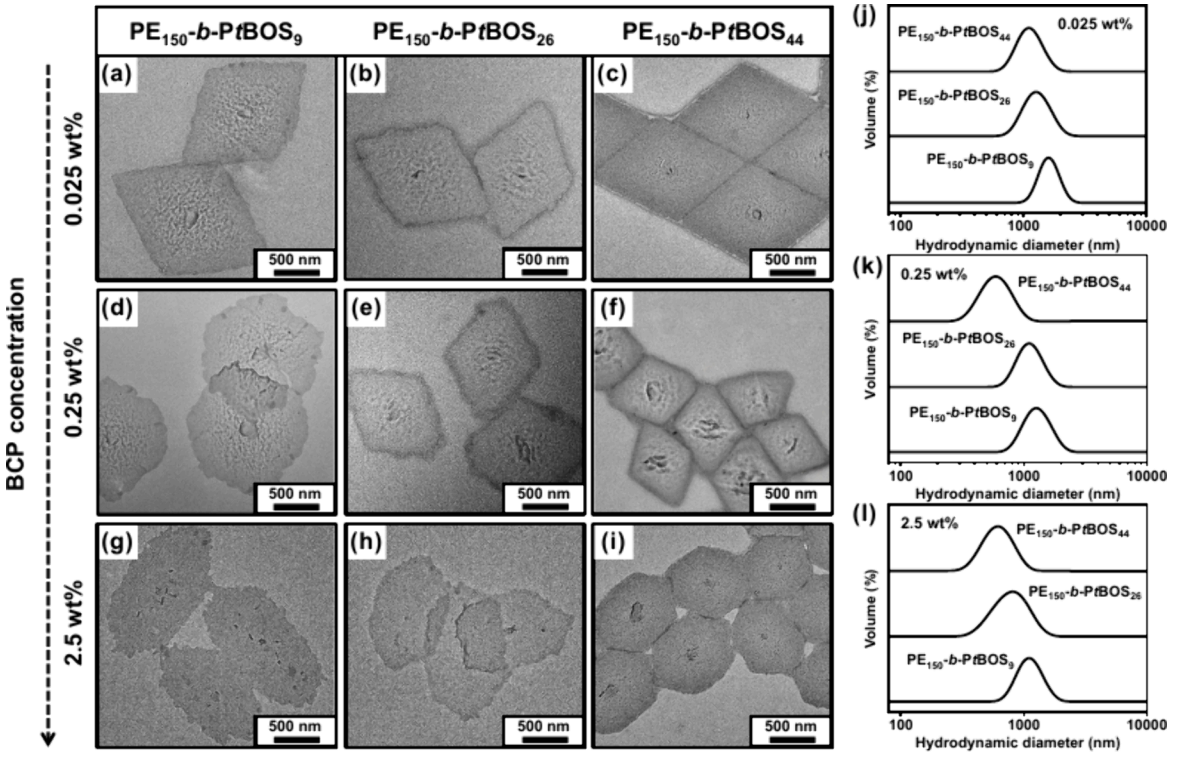

Figure 3. Representative TEM images of PE_{150}-*b*-P*t*BOS_x nanosheets obtained via the CDSA process in toluene at concentrations of (a–c) 0.025 wt %, (d–f) 0.25 wt %, and (g–i) 2.5 wt %. All the samples were annealed at 90 °C for 2.0 h, then naturally cooled to 25 °C in the oil bath, followed by aging at 25 °C for 24.0 h, and finally redispersed by oscillation for sample preparation. (j–l) Corresponding DLS results for PE_{150}-*b*-P*t*BOS_x nanosheets.

and PE_{150}-*b*-P*t*BOS_x BCPs are crystallizable (Figure S8). Specifically, the melting temperature (T_m) of PE_{150}-CTA homopolymer and all the PE_{150}-*b*-P*t*BOS_x BCPs was detected approximately 120 °C in the second heating run, which was consistent with the values reported in the literature.[50,51] Differently, the crystallization temperatures (T_c) of PE_{150}-CTA

https://doi.org/10.1021/acs.macromol.5c03517
Macromolecules XXXX, XXX, XXX−XXX

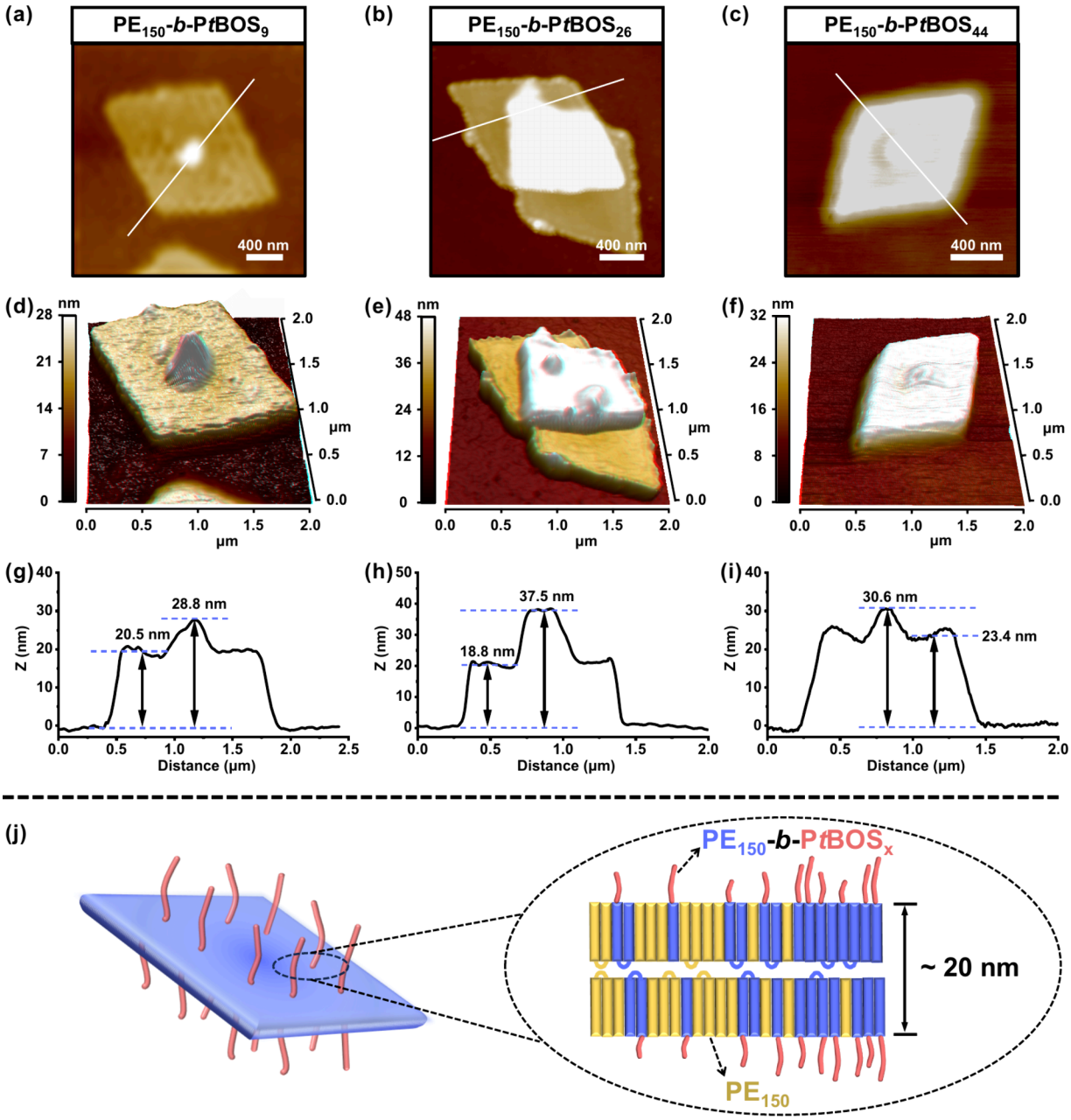

Figure 4. (a–c) 2D AFM images, (d–f) 3D AFM images, and (g–i) AFM height profiles of the PE_{150}-*b*-P*t*BOS$_x$ nanosheets obtained via CDSA in toluene at a concentration of 0.025 wt %. All of the samples were annealed at 90 °C for 2.0 h, then naturally cooled to 25 °C in the oil bath, followed by aging at 25 °C for 24.0 h, and finally redispersed by oscillation for sample preparation. (j) Schematic diagram of the structure of PE_{150}-*b*-P*t*BOS$_x$ nanosheets obtained via CDSA.

homopolymer and PE_{150}-*b*-P*t*BOS$_x$ BCPs were varied and detected between 115.2 and 72.5 °C in the cooling run. Specifically, the T_c of PE_{150}-*b*-P*t*BOS$_{44}$ was lower than those of PE_{150}-*b*-P*t*BOS$_{26}$ (105.8 °C), PE_{150}-*b*-P*t*BOS$_9$ (114.1 °C), and the PE_{150}-CTA precursor (115.2 °C). As DP_{PtBOS} increased, the gradual decrease in T_c could be attributed to the enhanced interruption and confinement of the relatively longer P*t*BOS blocks on the crystallization behavior of PE blocks in the BCPs. Overall, these WAXS and DSC results indicate that, although interrupted by P*t*BOS blocks, the PE blocks in PE_{150}-*b*-P*t*BOS$_x$ BCPs maintain crystallizability, and the BCPs can be used for the subsequent CDSA investigation.

CDSA Behavior of PE_{150}-*b*-P*t*BOS$_x$ BCPs under Different Annealing Temperatures

According to the principle of CDSA, toluene was employed as a selective solvent for PE_{150}-*b*-P*t*BOS$_x$ BCPs as it is a good solvent for the P*t*BOS block and a poor solvent for the PE block at room temperature (25 °C). Thus, the BCPs tended to self-assemble into nanostructures with P*t*BOS as the shell and PE as the core. Since the morphologies of the nanostructures self-assembled from the BCPs largely depended on the core-to-corona ratios, the BCPs with fixed DP_{PE} but varied DP_{PtBOS} were employed for the CDSA process. In this section, the effect of annealing temperature on the CDSA process was investigated, with the BCP concentration fixed at 0.25 wt %. In a typical procedure, the solid PE_{150}-*b*-P*t*BOS$_x$ BCPs and

https://doi.org/10.1021/acs.macromol.5c03517
Macromolecules XXXX, XXX, XXX−XXX

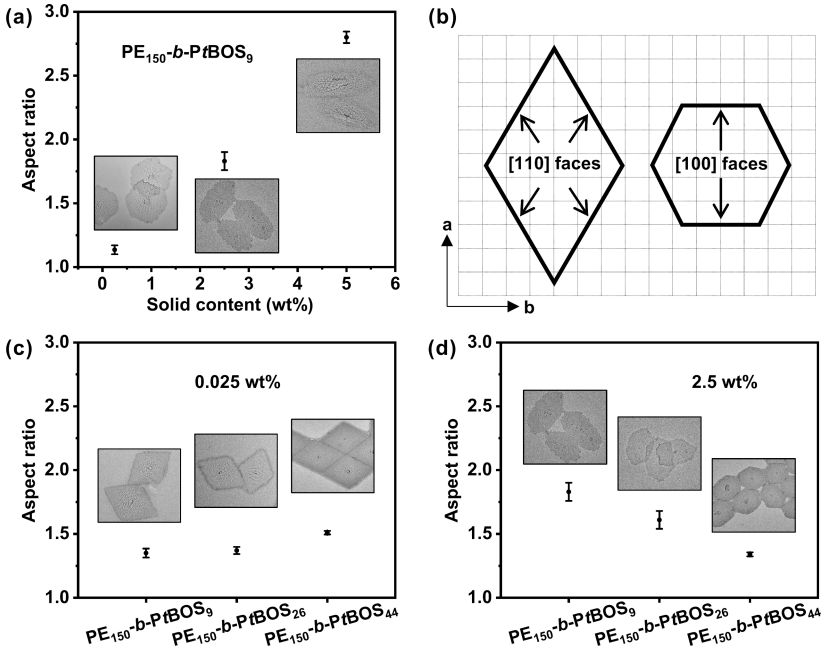

Figure 5. (a) Plot of aspect ratio vs concentration for PE_{150}-*b*-P*t*BOS_9 nanosheets. (b) Typical phase morphologies for PE single crystals. (c, d) Plot of aspect ratio vs DP_{PtBOS} for PE_{150}-*b*-P*t*BOS_x nanosheets.

toluene were sequentially placed in a 10 mL vial, initially forming a dispersion with stirring. Subsequently, the vial was sealed, and the dispersion was immersed in an oil bath (at 90, 92.5, 95, 100, or 130 °C) and annealed for 2.0 h, after which the heating and stirring were stopped. The dispersion was naturally cooled to 25 °C by leaving the vial in the oil bath, followed by aging at 25 °C for 24.0 h. Prior to sample preparation for characterization, the vial was subjected to a simple oscillation to ensure the uniformity of the dispersion.

After the CDSA process, the morphologies of the PE_{150}-*b*-P*t*BOS_x nanosheets were first monitored by transmission electron microscopy (TEM) measurement, as depicted in Figure 1a–i. Specifically, at a relatively low annealing temperature of 90 °C and a concentration of 0.25 wt %, the morphologies of the PE_{150}-*b*-P*t*BOS_x self-assemblies underwent a transformation from hexagonal to rhombic as DP_{PtBOS} increased, accompanied by a slight decrease in size. Furthermore, as the annealing temperature was increased to 92.5 and 95 °C, the sizes of the hexagonal and rhombic nanosheets increased significantly, which was clearly confirmed by the 2D plots depicting the statistical distribution of lengths and widths for these nanosheets (Figure 1j,k). However, as the annealing temperature was further increased to 100 and 130 °C, only fragmented nanosheets and an amorphous phase were observed in the corresponding TEM images (Figure S9).

Based on the results under different annealing temperatures, the CDSA process can be hypothesized to proceed as illustrated in Figure 1l. First, thermal annealing induces self-nucleation of the BCPs, with the majority of polymer chains dissolved as unimers, while the PE homopolymer and a minority of BCPs with relatively low DP_{PtBOS} tend to form crystal nuclei. With subsequent cooling, the unimers migrate rapidly toward crystal nuclei, growing uniformly from each crystal nucleus and eventually forming larger nanosheets via the aging process. Specifically, when the thermal annealing temperature is relatively low, more crystal nuclei are formed, resulting in smaller nanosheets. Simultaneously, an increase in annealing temperature reduces the number of formed nuclei, ultimately leading to an increase in nanosheet size. However, negligible nuclei remain upon further temperature elevation, theoretically enabling the formation of significantly larger nanosheets, which may be unstable and tend to fragment during growth. Moreover, given that few crystal nuclei are ultimately generated, not all of the dissolved BCPs can participate in the growth process, leading to the observation of an amorphous phase in the corresponding TEM images. Thus, just by modulating the annealing temperature, we achieved the fabrication of nanosheets with tunable sizes via a simple one-pot CDSA process. This process is analogous to the self-seeding method in the "living" CDSA process,[45] which, however, requires the preliminary preparation of seed crystals.

To prove the above deduction, we attempted to capture the crystal nuclei by preparing the TEM samples just after annealing and prior to cooling. However, due to the rapid cooling during the TEM sampling process by immersing the copper grid into the hot dispersions and subsequent taking out thereof, it was unavoidable to induce the fast and uncontrolled growth of BCP unimers on the crystal nuclei (Figure S10). What was actually observed might be the derived crystal structure after the growth of unimers from crystal nuclei but different from those after the full CDSA process in Figure 1a–i, and thus the intrinsic morphologies of the original crystal nuclei could not be directly captured. For example, after annealing at 90 °C for 2.0 h, the TEM images of hot dispersions prior to cooling indicated that the rhombic lamellar crystals with nonuniform sizes were generated for PE_{150}-*b*-P*t*BOS_9 and PE_{150}-*b*-P*t*BOS_{26} (Figure S10a,b). After annealing at 95 °C for 2.0 h, the TEM images showed more irregular morphologies than those after annealing at 90 °C (Figure S10d,e). Furthermore, after annealing at 130 °C for 2.0 h, almost no regular morphologies could be discriminated (Figure S10g,h). Especially, for PE_{150}-*b*-P*t*BOS_{44}, irregular aggregates were consistently observed (Figure S10c,f,i). Nevertheless, after annealing from 90 to 130 °C, the evolution

https://doi.org/10.1021/acs.macromol.5c03517
Macromolecules XXXX, XXX, XXX−XXX

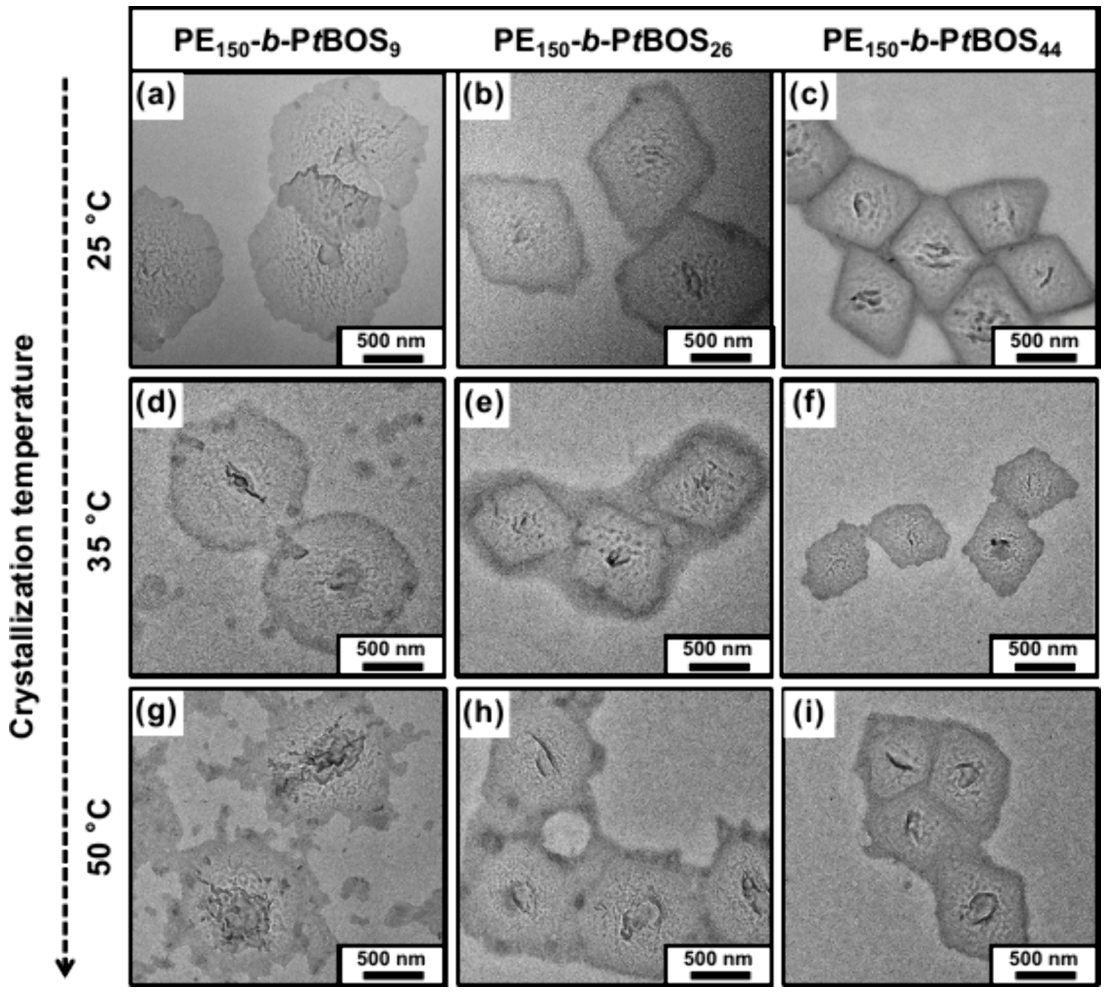

Figure 6. Representative TEM images of PE_{150}-*b*-P*t*BOS_x nanosheets obtained via the CDSA process in toluene at a concentration of 0.25 wt %. All of the samples were annealed at 90 °C for 2.0 h, then naturally cooled to (a–c) 25 °C, (d–f) 35 °C, and (g–i) 50 °C in the oil bath, followed by aging at the corresponding temperatures for 24.0 h, and finally redispersed by oscillation for sample preparation.

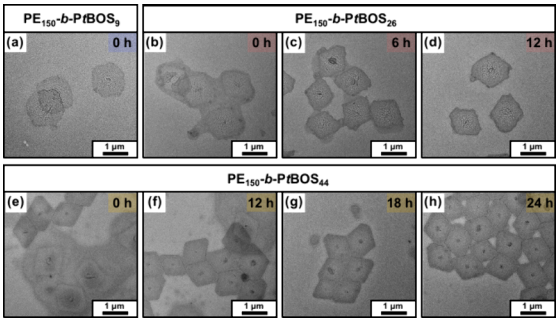

Figure 7. Representative TEM images of PE_{150}-*b*-P*t*BOS_x nanosheets obtained via the CDSA process in toluene at a concentration of 0.25 wt %. The samples were annealed at 90 °C for 2.0 h, then naturally cooled to 25 °C in an oil bath, subsequently aged at 25 °C for different times, and finally redispersed by oscillation for sample preparation.

of TEM images qualitatively illustrated that the number of crystal nuclei gradually decreased, leading to the uneven growth of unimers and the formation of more irregular morphologies. Alternatively, to verify the existence of crystal nuclei, the dynamic light scattering (DLS) measurement was performed at 90 °C and the sizes of the original crystal nuclei at 90 °C were detected from 70 to 40 nm with increasing DP_{PtBOS} (Figure S11). However, the typical DLS equipment was limited by its maximum measurable temperature of 90 °C. Nevertheless, the DLS results at 90 °C confirm the presence of crystal nuclei, which exhibit a dependence on DP_{PtBOS}. Additionally, it should be noted that DP_{PtBOS} and T_c exhibit a correlation, as shown by the DSC results in Figure S8. Thus, the sizes of crystal nuclei also exhibit dependence on T_c. That is, the lower the T_c of the BCPs, the smaller the crystal nuclei, the more irregular morphologies at elevated temperatures are generated, and finally incomplete crystallization and relatively more irregular and smaller nanosheets after the CDSA process are observed. For example, the PE_{150}-*b*-P*t*BOS_{44} has a T_c of 72.5 °C, shows the most irregular morphologies at elevated temperatures, and yields nanosheets with the most irregular morphologies and smallest sizes after CDSA. Thus, the TEM images and DLS results captured at elevated temperatures (Figures S10 and S11), the TEM images after the CDSA process (Figure 1a–i), as well as the DSC results (Figure S8), comprehensively support the core inference that an increase in the annealing temperature leads to a decrease in the number of crystal nuclei and an increase in their size.

Furthermore, to probe the internal molecular packing, the hexagonal/rhombic nanosheets with varying sizes, obtained via the CDSA process at different annealing temperatures, were collected via solvent evaporation at room temperature and

https://doi.org/10.1021/acs.macromol.5c03517
Macromolecules XXXX, XXX, XXX–XXX

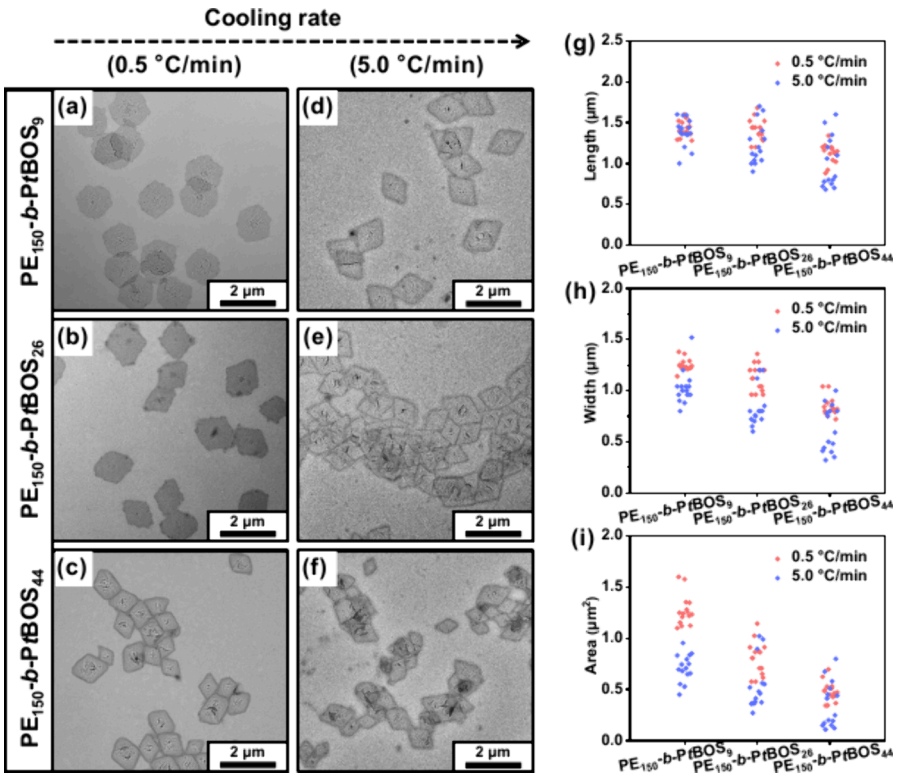

Figure 8. (a–f) Representative TEM images of PE_{150}-*b*-P*t*BOS_x nanosheets obtained via the CDSA process in toluene at a concentration of 0.25 wt %. All samples were annealed at 90 °C for 2.0 h, then cooled to 25 °C either by natural cooling in the oil bath or in air (corresponding to cooling rates of about 0.5 and 5.0 °C/min, respectively), followed by aging at 25 °C for 24.0 h, and finally redispersed by oscillation for sample preparation. (g–i) Numerical distribution plots of length, width, and area versus DP_{PtBOS} for PE_{150}-*b*-P*t*BOS_x nanosheets, as statistically obtained from TEM images.

further characterized via a WAXS measurement. As shown in Figure 2a–c, all PE_{150}-*b*-P*t*BOS_x BCPs before the CDSA process exhibit two distinct crystalline peaks corresponding to the PE blocks, peaking at 2θ = 21.6° and 2θ = 24.0°, respectively. After the CDSA process at an annealing temperature of 90 °C and a concentration of 0.25 wt %, the corresponding nanosheets display a marked intensity enhancement of the crystalline peak at 2θ = 21.6°, with the crystalline peak at 2θ = 24.0° exhibiting a sharper profile. Meanwhile, the broad scattering peak at 2θ = 18.1° attributed to the amorphous P*t*BOS segments nearly vanishes for both PE_{150}-*b*-P*t*BOS_{26} and PE_{150}-*b*-P*t*BOS_{44}. These results indicate that the PE_{150}-*b*-P*t*BOS_x BCPs were arranged into highly ordered nanostructures after the CDSA process at an annealing temperature of 90 °C. By comparison, the nanostructures obtained via the CDSA process at an annealing temperature of 130 °C retain a broad scattering peak corresponding to the amorphous P*t*BOS blocks, and the crystalline peaks for the PE blocks are significantly attenuated. These findings are consistent with the corresponding TEM results (Figure S9d–f), collectively indicating that the internal structures of the self-assemblies fail to achieve high order. In addition, the first heating DSC curves of the aforementioned samples provide further confirmation (Figure 2d–f). That is, the PE_{150}-*b*-P*t*BOS_x BCPs after the CDSA process at 90 °C annealing exhibit the largest melting peak areas and melting enthalpies compared with both the samples before the CDSA process and those subjected to the CDSA process at 130 °C annealing, further indicating that the nanosheets possess nanostructures with the highest degree of order under this condition.

CDSA Behavior of PE_{150}-*b*-P*t*BOS_x BCPs at Different Concentrations

Following the clarification of the effects of annealing temperature and DP_{PtBOS} on the morphologies of the self-assemblies, we further investigated the variation patterns of the self-assemblies under different BCP concentrations to achieve a higher level of control and enhance practical application potential.

Similarly, the morphologies of the resulting nanostructures were first monitored by TEM measurement. As shown in Figure 3a, the PE_{150}-*b*-P*t*BOS_9 self-assemblies obtained via the CDSA process at a relatively low concentration of 0.025 wt % exhibit uniform rhombic nanosheets, with a length of 1.90 ± 0.10 μm and a width of 1.40 ± 0.10 μm. In comparison, PE_{150}-*b*-P*t*BOS_{26} and PE_{150}-*b*-P*t*BOS_{44} exhibit smaller rhombic nanosheets, with lengths of 1.63 ± 0.02 μm and 1.69 ± 0.01 μm, and widths of 1.20 ± 0.05 μm and 1.15 ± 0.05 μm, respectively (Figure 3b,c). As the concentration was further increased to 0.25 wt %, the PE_{150}-*b*-P*t*BOS_9 self-assemblies evolved into a hexagonal morphology, while the PE_{150}-*b*-P*t*BOS_{26} and PE_{150}-*b*-P*t*BOS_{44} self-assemblies maintained the rhombic ones (Figure 3d–f). When the concentration was further increased to 2.5 wt %, all the nanosheets evolved into a hexagonal morphology (Figure 3g–i). Generally, the sizes of the nanosheets significantly decrease with the increase in DP_{PtBOS} at all three concentrations. The sizes of nanostructures at various concentrations were also characterized by DLS, which was aimed at further revealing the effects of DP_{PtBOS} and the concentration on self-assembly behavior, and the corresponding results are presented in Figure 3j–l. Similarly,

https://doi.org/10.1021/acs.macromol.5c03517
Macromolecules XXXX, XXX, XXX–XXX

it is observed that the sizes of the nanosheets significantly decrease as DP_{PtBOS} increases under varying concentrations, which is generally consistent with that from the TEM images. However, both the TEM and DLS results show that the concentration has a less significant effect on the sizes of nanosheets of the same BCP. This is most probably due to the shorter solvophilic segments lacking the capacity to maintain the stability of the core, thereby driving the BCPs to assemble into larger structures to reduce their overall free energy. This tendency was further verified by a precipitation experiment, i.e., the CDSA system (0.25 wt %) was first annealed at 90 °C for 2.0 h in an oil bath, then the vials were taken out, and the dispersions were statically cooled in air to facilitate the observation of precipitation. The photos in Figure S12 show that, as DP_{PtBOS} increases, the time for obvious precipitation to occur extended from 8.0 min (for PE_{150}-CTA) to 24.0 h (for PE_{150}-*b*-P*t*BOS_{44}). As noted in the previous section, before the sampling for TEM observation, the dispersions had been redispersed by simple oscillation. Thus, although the precipitates were formed after long-time standing, the TEM images still showed uniform sizes and regular morphologies, especially in low-magnification TEM observations over a large field of view (Figure S13), meaning that the self-assemblies were weakly aggregated and could be redispersed (Figure 3), rather than irreversible precipitated aggregates. Similarly, large-area uniform and regular nanosheets can also be observed in Figure 8a−c with low magnification, which are presented and further discussed in detail in a subsequent section. In contrast, the precipitates generated from the PE_{150}-CTA homopolymer were irreversible and could not be redispersed due to the absence of the P*t*BOS block as a stabilizer (Figure S14). Additionally, another phenomenon is observed in these nanosheets. That is, the morphological evolution from uniform hexagonal nanosheets to rhombic nanosheets can be induced by either decreasing the concentration or increasing the DP_{PtBOS}. To the best of our knowledge, the realization of fabricating nanosheets that exhibit both size controllability and the ability to undergo bidirectional morphological transformation between hexagonal and rhombic morphologies has rarely been reported.

Furthermore, the nanosheets were also characterized by an atomic force microscopy (AFM) measurement (Figures 4 and S15). The AFM height profiles revealed that the sheet-like structures have a uniform thickness (≈20 nm), irrespective of variations in DP_{PtBOS} or concentration. Given that the nanosheets were primarily derived from the effective stacking of crystallizable PE block, this consistency in thickness values suggests that the molecular stacking mode remains nearly unchanged. Additionally, the AFM height profiles revealed that the nanosheet surfaces are not flat but instead exhibit a slight concavity between the center and edge regions. For instance, in Figure 4g, the central region of the nanosheet shows a height of approximately 28.8 nm and the edge region is around 22.0 nm, while the thinnest point between these two regions has a thickness of only 19.2 nm. Similarly, the slightly concave morphology observed between their central and edge regions has also been reported for other BCPs in the literature.[32,52−54] Herein, this phenomenon can be attributed to the heterogeneous distribution of the PE_{150} homopolymer and PE_{150}-*b*-P*t*BOS_x BCPs within the nanosheets. As already noted, although the end-group conversion efficiencies of both PE-Vinyl and subsequent PE-OH were nearly 100%, the PE initially prepared via coordination polymerization contained approximately 85% PE-Vinyl. Thus, the subsequent BCPs should contain a small amount of PE_{150} homopolymer. Due to the hindrance of the amorphous P*t*BOS segments in PE_{150}-*b*-P*t*BOS_x, its crystallization ability is weaker than that of PE_{150} homopolymer, a conclusion supported by the above WAXS and DSC data (Figures S7 and S8). Therefore, the PE_{150} homopolymer, with its stronger crystallization ability, preferentially crystallized to form crystal nuclei during the CDSA process. As the PE_{150} homopolymer was consumed, the proportion of PE_{150}-*b*-P*t*BOS_x in the dissolved PE_{150}-*b*-P*t*BOS_x/PE_{150} mixture gradually increased. This led to more PE_{150}-*b*-P*t*BOS_x being incorporated into nanosheets during the later growth stage, resulting in their distribution at the nanosheet edges. That is to say, in combination with the TEM images (Figure 3a−i), the variations in DP_{PtBOS} or concentration dominantly affect the lateral growth of the nanosheets. As for the central height of 28.8 nm, it can be attributed to the facile aggregation of additional PE_{150} homopolymer or PE_{150}-b-PtBOS_x BCPs with relatively low DP_{PtBOS} on the surface of primary crystal nuclei, due to the absence of PtBOS segments in this region. Consistent with these deductions, distinct protrusions are detected at the center of each nanosheet in the three-dimensional (3D) AFM images (Figure 4d−f), and the height of these protrusions can be quantified from the corresponding AFM height profiles (Figures 4g−i and S15c,d). Notably, the darkened crystal nuclei are also consistently observed in the corresponding TEM images of the nanosheets (Figure 3a−i).

In fact, the aforementioned thickness of the nanosheets can be further analyzed as follows. Previous works reported that the PE always formed single crystals with a thickness of around 10 nm in dilute solution, regardless of the molecular weight.[55−57] According to the formula $L = nl \sin\frac{\theta}{2}$ (l = 0.154 nm, the single bond length; θ = 109.5°, the bond angle), it can be derived that 10 nm only corresponds to the contour length of PE_{66}. Thus, it can be deduced that the PE chains are arranged into crystalline lattices via single-fold or multiple-fold conformations. Following this rule, Xu et al. measured the thickness of PE_{100}-*b*-poly(*tert*-butyl acrylate)$_{48}$/PE_{52} nanosheets as 25 nm in *N*,*N*-dimethylformamide (DMF) and proposed a bilayer crystal structure model.[36] Similarly, for our PE_{150}-*b*-P*t*BOS_x BCP system, a thickness around 20 nm can also be regarded as a bilayer crystal structure of PE, stabilized by a single outer P*t*BOS layer (Figure 4j). According to the GPC results (Figure S6), the molecular weight distribution of PE blocks is relatively broad, with DP_{PE} values ranging from 10 to 1700. Nevertheless, PE chains of varying block lengths do not affect the uniformity of the nanosheets, as relatively shorter PE chains tend to adopt a single-fold conformation, while relatively longer PE chains favor a multiple-fold conformation.

Besides the controlled preparation of uniform hexagonal/rhombic nanosheets with precise sizes, it is also observed that the aspect ratio of these nanosheets can be tuned by varying the concentration and DP_{PtBOS} (Figure 3). Based on these TEM images, we selected several groups of nanosheets and compared their corresponding aspect ratios. For example, in Figure 5a, the calculated aspect ratio of PE_{150}-*b*-P*t*BOS_9 nanosheets increases from 1.1 to 1.8 and then to 2.8 as the concentration increases from 0.25 to 2.5 wt % and further to 5 wt % (Figures 3d,g and S16), indicating that the concentration exerts a significant influence on the aspect ratio of 2D CDSA nanosheets. This variation in the nanosheet aspect ratio may

https://doi.org/10.1021/acs.macromol.5c03517
Macromolecules XXXX, XXX, XXX−XXX

arise from differing crystallization rates of different crystalline facets (Figure 5b). Previous studies have demonstrated that PE single crystals grown from extremely dilute solutions are bounded by four (110) faces.[58,59] As the concentration increases, two truncated (100) faces appear. Furthermore, the axial ratio of PE single crystals increases at higher concentrations and crystallization temperatures with the crystals growing more elongated along the *b*-axis. The curvature of the (100) faces becomes more pronounced as the axial ratio continues to increase. Analogously, the crystallization behavior of PE_{150} was investigated under similar CDSA conditions, i.e., annealing in toluene at 90 °C for 2.0 h, followed by natural cooling in the oil bath and subsequent aging at 25 °C for 24.0 h. As shown in Figure S14a,c, the PE_{150} single crystals transform from rhombic to hexagonal shapes with increasing the concentration, which is consistent with the reports in the literature.[58,59] However, most PE_{150} single crystals exhibit stacked and dense nanosheets (Figure S14b,d), which cannot be redispersed due to the high crystallization ability of the PE_{150} homopolymer. Once the P*t*BOS blocks were introduced, the crystallization behavior of PE blocks could be modulated and the PE_{150}-*b*-P*t*BOS_x nanosheets could be readily redispersed even after precipitation. Additionally, as an example, the selected area electron diffraction (SAED) analysis of the PE_{150}-*b*-P*t*BOS_9 nanosheets was also performed (Figure S17). From the diffraction characteristics, it is possible to clearly distinguish that the diffraction pattern presents several discrete diffraction spots with a regular arrangement and distinct boundaries. The characteristic diffraction spots with higher intensity were calibrated using crystal plane indices, corresponding to the (110) and (200) planes of the PE orthorhombic crystal system, respectively. The SAED result effectively confirmed that the lamellae formed by PE_{150}-*b*-P*t*BOS_9 are single-crystalline structures, rather than polycrystalline aggregates with random orientations. These observations on PE single crystals, which include their concentration-dependent morphological evolution, variations in axial ratio, and the stacking phenomenon caused by rapid crystallization, lay the foundation for interpreting the more complex aspect ratio regulation mechanism of PE_{150}-*b*-P*t*BOS_x nanosheets—one of the key points investigated in this study. Correspondingly, Figure 5a reveals that the curvature of the (100) faces of hexagonal nanosheets increases as the concentration rises, accompanied by the promotion of the growth for nanosheets along the *b*-axis and a corresponding increase in the aspect ratio. Furthermore, Figure 5c,d present the plots of the nanosheet aspect ratio against DP_{PtBOS} at concentrations of 0.025 and 2.5 wt %, respectively. As DP_{PtBOS} increases, both the increase in the aspect ratio of rhombic nanosheets and the reduction in that of hexagonal nanosheets can be attributed to the suppressed growth of nanosheets along the *b*-axis—a phenomenon that may arise from the influence of the amorphous P*t*BOS blocks on the crystallization behavior of PE segments.

CDSA Behavior of PE_{150}-*b*-P*t*BOS_x BCPs under Additional Factors

Beyond the well-established key variables governing nanosheet formation, specifically, concentration, annealing temperature, and DP_{PtBOS}, a comprehensive understanding of the structural diversity of such nanosheets necessitates an assessment of additional factors.

First, the effect of crystallization temperature on morphological evolution was investigated. Specifically, with a concentration of 0.25 wt %, an annealing temperature of 90 °C, a cooling mode of natural cooling in the oil bath, and the aging time of 24.0 h fixed, a series of nanosheets were prepared via the CDSA process with crystallization temperatures set at 25, 35, and 50 °C, respectively (Figure 6). At a relatively low crystallization temperature of 25 °C, TEM results show that the obtained nanosheets exhibit distinct morphological boundaries with almost no residual amorphous phase observed. As the crystallization temperature increases to 35 °C, the morphological boundaries of the PE_{150}-*b*-P*t*BOS_x nanosheets become blurred, and interfacial adhesion occurs between adjacent nanosheets. When the crystallization temperature is further increased to 50 °C, the aforementioned boundary blurring and adhesion phenomena are significantly exacerbated. Obviously, it is found that nanosheets with well-defined morphological contours and no interfacial adhesion can be produced only at a crystallization temperature of 25 °C. This regulatory mechanism can be analyzed from both thermodynamic and kinetic perspectives. Regarding the effect of crystallization temperature, a relatively low temperature (25 °C) can effectively suppress the disordered diffusion of segments, promote the oriented arrangement of polymer crystal segments along specific crystal planes of nuclei, and thereby form ordered crystalline structures with clear boundaries. However, when the crystallization temperature is increased to 35−50 °C, the thermal motion of molecular chains intensifies, accelerating the disordered diffusion of segments. This readily results in random adsorption on the surface of the nuclei and interfacial fusion between adjacent nanosheets.

Meanwhile, the effect of aging time was also investigated. Specifically, with a concentration of 0.25 wt %, an annealing temperature of 90 °C, natural cooling in the oil bath, and a crystallization temperature of 25 °C fixed, a series of nanosheets were prepared via the CDSA process with an aging time of 0∼24.0 h. As shown in Figure 7, as DP_{PtBOS} increases, the critical aging time to achieve stable nanosheet morphologies exhibits a significant upward trend. Specifically, the sample PE_{150}-*b*-P*t*BOS_9 with the lowest DP_{PtBOS} requires 0 h of aging time to form well-defined nanosheets, whereas for the samples with a moderate (PE_{150}-*b*-P*t*BOS_{26}) and the highest DP_{PtBOS} (PE_{150}-*b*-P*t*BOS_{44}), the critical aging times are extended to 12.0 and 24.0 h, respectively. In addition, for PE_{150}-*b*-P*t*BOS_{26} and PE_{150}-*b*-P*t*BOS_{44}, prolonged aging gradually eliminates the residual amorphous phase in the corresponding TEM images. Clearly, the aging time needs to match the DP_{PtBOS} value. An appropriate aging time can provide a sufficient kinetic window, ensuring that amorphous parts fully diffuse to the surface of nuclei and participate in ordered crystallization, thus ensuring the regularity of nanosheet' outlines. That is, the aging process appears to remain essential, especially for the BCPs with relatively high DP_{PtBOS} values due to the relatively slow crystallization process.

Additionally, the effect of the cooling rate on morphological evolution was investigated. To this aim, two cooling protocols were adopted: natural cooling by maintaining the system in the oil bath (∼0.5 °C/min, Figure 8a−c) and in air (∼5.0 °C/min, Figure 8d−f). Key findings reveal that increasing the cooling rate from 0.5 to 5.0 °C/min not only leads to a significant reduction in both nanosheet size and uniformity but also induces a shape transition from hexagonal to rhombic

https://doi.org/10.1021/acs.macromol.5c03517
Macromolecules XXXX, XXX, XXX−XXX

nanosheets. Statistical distribution plots of length, width, and area further demonstrate that, as the cooling rate increases, the overall size of the nanosheets decreases, and their heterogeneity becomes pronounced (Figure 8g–i). Additionally, small regions of the amorphous phase are observed in the corresponding TEM images. Given that the segmental diffusion rate exhibits an exponential dependence on temperature, the thermal mobility of unimers is significantly diminished by rapid cooling, impairing the ability of crystalline segments to quickly diffuse to the surface of growing nuclei and align in an ordered manner. Consequently, although crystal nuclei form successfully, their growth is incomplete. Some nuclei develop into small nanosheets due to insufficient growth, while others evolve into slightly larger particles driven by localized high concentrations of polymer chains, ultimately yielding poor overall uniformity, with a small fraction of polymer chains failing to diffuse in time and thus remaining in an amorphous phase. Based on the above results, we conclude that the key parameter affecting the uniformity of nanoparticles might be the cooling rate (kinetics process) rather than the uniformity of BCPs (thermodynamics process). Again, due to the slowed crystallization process, the BCPs with different lengths of PE blocks can all be rearranged into crystals either by single-fold or multiple-fold configurations. Thus, the negative effect of the broad molecular weight distribution of PE blocks is negated, enabling the formation of uniform nanosheets. As for the morphological transition from hexagonal to rhombic, it can be proposed that, analogous to the transformation observed from Figure 3d to Figure 3a, increasing the cooling rate has an effect similar to that of reducing the concentration: both reduce the number of thermally mobile umimers, ultimately leading to the disappearance of the (100) faces.

CONCLUSIONS

To address the technical challenges of CDSA for 2D nanosheet preparation, including the low concentration, cumbersome processes, and difficulty in regulating morphology, size, and aspect ratio, we employed a one-pot CDSA strategy with a "heating–cooling-aging" protocol, using PE-*b*-P*t*BOS as the research model, to enable controlled synthesis of uniform hexagonal/rhombic nanosheets across a wide concentration range from 0.025 to 5.0 wt %. The effects of critical parameters, such as DP_{PtBOS}, concentration, annealing temperature, crystallization temperature, aging time, and cooling rate, on the morphologies, sizes, and aspect ratios of the nanosheets were systematically investigated, yielding several key findings. First, the synergistic regulation of DP_{PtBOS} and annealing temperature significantly modulates the overall sizes of the nanosheets. Second, the precise tuning of the aspect ratios of hexagonal/rhombic nanosheets can be readily achieved through the regulation of the concentration or DP_{PtBOS}. Third, bidirectional morphological transition between hexagonal and rhombic nanosheets can be achieved by regulating the concentration, DP_{PtBOS}, and cooling rate. Collectively, this one-pot protocol enabled "size tunability, aspect ratio controllability, and bidirectional morphological transition between hexagonal and rhombic structures". This work not only deepens the fundamental understanding of the CDSA process but also enriches the routes to anisotropic nanostructures and the concerned applications.

ASSOCIATED CONTENT

Supporting Information

The Supporting Information is available free of charge at https://pubs.acs.org/doi/10.1021/acs.macromol.5c03517.

Experimental procedures for the synthesis and additional characterization data, including Figures S1–S17 (PDF)

AUTHOR INFORMATION

Corresponding Author

Guowei Wang − *State Key Laboratory of Molecular Engineering of Polymers, Department of Macromolecular Science, Fudan University, Shanghai 200438, China;* orcid.org/0000-0003-2595-8269; Email: gwwang@fudan.edu.cn

Authors

Jiali Wu − *State Key Laboratory of Molecular Engineering of Polymers, Department of Macromolecular Science, Fudan University, Shanghai 200438, China*

Boyang Shi − *State Key Laboratory of Molecular Engineering of Polymers, Department of Macromolecular Science, Fudan University, Shanghai 200438, China*

Ding Shen − *State Key Laboratory of Molecular Engineering of Polymers, Department of Macromolecular Science, Fudan University, Shanghai 200438, China*

Hanyu Lv − *State Key Laboratory of Molecular Engineering of Polymers, Department of Macromolecular Science, Fudan University, Shanghai 200438, China*

Complete contact information is available at: https://pubs.acs.org/10.1021/acs.macromol.5c03517

Notes

The authors declare no competing financial interest.

ACKNOWLEDGMENTS

We appreciate the financial support of this research by the National Natural Science Foundation of China (22271058).

REFERENCES

(1) Jin, R. M.; Zhang, G. C.; Tang, L. L.; Li, M. Y.; Yang, M.; Li, J. L.; Wang, Z. M.; Guan, F. X. Active-Targeting Biomimetic Polymer Nanoparticles for NIR Fluorescence Imaging and Enhanced Chemo-Sonodynamic Therapy of Cancer. *ACS Appl. Nano Mater.* **2024**, *7* (4), 3968–3976.

(2) Haidar, L. L.; Bilek, M.; Akhavan, B. Surface Bio-Engineered Polymeric Nanoparticles. *Small* **2024**, *20* (21), 33.

(3) Li, Y.; Scheerstra, J. F.; Liu, Y.; Wauters, A. C.; Wang, J.; Wu, H.; Patino, T.; Llopis-Lorente, A.; van Hest, J. C. M.; Abdelmohsen, L. K. E. A. Facile Synthesis of Rapamycin-Loaded PEG-*b*-PLA Nanoparticles and Their Application in Immunotherapy. *J. Polym. Sci.* **2024**, *62* (10), 2215.

(4) Du, F.; Rische, C. H.; Li, Y.; Vincent, M. P.; Krier-Burris, R. A.; Qian, Y.; Yuk, S. A.; Almunif, S.; Bochner, B. S.; Qiao, B.; Scott, E. A. Controlled Adsorption of Multiple Bioactive Proteins Enables Targeted Mast Cell Nanotherapy. *Nat. Nanotechnol.* **2024**, *19* (5), 698–704.

(5) Soheilian, S.; Jordan, B.; Hatton, F. L.; Hunsicker, E.; Zhou, Z. Impact of Size and UV-Ageing of Polystyrene Nanoparticles on Copper (II) Adsorption: Kinetics and Isotherms in Aquatic Environments. *Environ. Sci. Nano* **2025**, *12* (1), 548–562.

(6) Rotolo, L.; Vanover, D.; Bruno, N. C.; Peck, H. E.; Zurla, C.; Murray, J.; Noel, R. K.; O'Farrell, L.; Araínga, M.; Orr-Burks, N.; et al.

Species-Agnostic Polymeric Formulations for Inhalable Messenger RNA Delivery to the Lung. *Nat. Mater.* **2023**, *22* (3), 369−379.
(7) Heyns, I. M.; Arora, M.; Ganugula, R.; Allamreddy, S. R.; Tiwari, S.; Shah, D. K.; Basu, R.; Kumar, M. R. Polyester Nanoparticles with Controlled Topography for Peroral Drug Delivery Using Insulin as a Model Protein. *ACS Nano* **2024**, *18* (18), 11863−11875.
(8) Boott, C. E.; Nazemi, A.; Manners, I. Synthetic Covalent and Non-Covalent 2D Materials. *Angew. Chem., Int. Ed.* **2015**, *54* (47), 13876−13894.
(9) Qin, H.; Li, F.; Wang, D.; Lin, H.; Jin, J. Organized Molecular Interface-Induced Noncrystallizable Polymer Ultrathin Nanosheets with Ordered Chain Alignment. *ACS Nano* **2016**, *10* (1), 948−956.
(10) Yan, N.; Liu, X.; Zhu, J.; Zhu, Y.; Jiang, W. Well-Ordered Inorganic Nanoparticle Arrays Directed by Block Copolymer Nanosheets. *ACS Nano* **2019**, *13* (6), 6638−6646.
(11) Wu, J.; Liu, S.; Huang, J.; Cui, Y.; Ma, P.; Wu, D.; Matyjaszewski, K. Fabrication of Advanced Hierarchical Porous Polymer Nanosheets and Their Application in Lithium-Sulfur Batteries. *Macromolecules* **2021**, *54* (6), 2992−2999.
(12) Li, X.-Y.; Zeng, H.; Hu, H.-M.; Sun, L.-J.; Zhang, J.-L.; Wang, X.-f. Multiterpyridyl Ligand/Cadmium (II) Coordination Polymer Nanosheets for Recoverable Luminescent Sensors. *ACS Appl. Nano Mater.* **2022**, *5* (5), 7113−7122.
(13) Cai, J.; Chua, X. W.; Li, C.; Grune, J.; Ghosh, P.; Ding, Y.; MacKenzie, H. K.; Qiu, H.; Greenham, N. C.; Rao, A.; Manners, I. Uniform Conjugated Polymer Rectangular Platelets Exhibiting Long-Range Exciton Diffusion. *Nat. Mater.* **2025**, *24* (12), 1985−1992.
(14) Sun, X.-L.; Liu, D.-M.; Pei, S.; Li, K.-K.; Wan, W.-M. Versatile Method to Expand the Morphology Library of Block Copolymer Solution Self-Assemblies with Tubular Structures. *ACS Macro Lett.* **2016**, *5* (10), 1180−1184.
(15) Cho, A.; La, Y.; Shin, T. J.; Park, C.; Kim, K. T. Structural Requirements of Block Copolymers for Self-Assembly into Inverse Bicontinuous Cubic Mesophases in Solution. *Macromolecules* **2016**, *49* (12), 4510−4519.
(16) Shen, D.; Shi, B.; Zhou, P.; Li, D.; Zhu, W.; Wang, G. All-Polylactones Nano-Objects Prepared by a One-Pot Ring-Opening Polymerization-Induced Self-Assembly Process. *Macromolecules* **2024**, *57* (19), 8970−8982.
(17) Wang, J.; Cao, M.; Zhou, P.; Wang, G. Exploration of a Living Anionic Polymerization Mechanism into Polymerization-Induced Self-Assembly and Site-Specific Stabilization of the Formed Nano-Objects. *Macromolecules* **2020**, *53* (8), 3157−3165.
(18) Tan, Z.; Lan, W.; Hou, Z.; Wang, K.; Li, Y.; Xu, J.; Luo, X.; Zhang, L.; Zhu, J. Flow-Induced Micellar Morphological Transformation in Microfluidic Chips under Nonequilibrium State: From Aggregates to Spherical Micelles. *Langmuir* **2020**, *36* (19), 5377−5384.
(19) Zhang, J.; Zhou, P.; Shi, B.; Li, P.; Wang, G. High-Efficient Access to Inverse Morphologies via Living Anionic Polymerization-Mediated Polymerization-Induced Cooperative Assembly. *Macromolecules* **2023**, *56* (15), 5743−5753.
(20) Lefley, J.; Huband, S.; Becer, C. R. Access to Self-Assembled Poly(2-Oxazoline)s through Cationic Ring Opening Polymerization-Induced Self-Assembly (CROPISA). *Macromolecules* **2025**, *58* (15), 7744−7756.
(21) Zhang, J.; Shi, B.; Wu, X.; Fang, X.; Liang, X.; Peng, Z.; Wang, G. Expanding the Scope of Self-Assembly: Heat-Induced Self-Assembly of Block Copolymers with High Solids. *Macromolecules* **2025**, *58* (10), 4985−5000.
(22) Kuo, C.-C.; Shao, S.-W.; Puneet, P.; Yashima, E.; Ho, R.-M. Induced Circularly Polarized Luminescence of Dynamically Racemic Luminophores Assisted by Formation of Helical Phase via Self-Assembly of Chiral Block Copolymers. *Macromolecules* **2025**, *58* (15), 8308−8315.
(23) Fu, J.; Luan, B.; Yu, X.; Cong, Y.; Li, J.; Pan, C.; Han, Y.; Yang, Y.; Li, B. Self-Assembly of Crystalline-Coil Diblock Copolymer in Solvents with Varying Selectivity: From Spinodal-Like Aggregates to Spheres, Cylinders, and Lamellae. *Macromolecules* **2004**, *37* (3), 976−986.
(24) Hurst, P. J.; Graham, A. A.; Patterson, J. P. Gaining Structural Control by Modification of Polymerization Rate in Ring-Opening Polymerization-Induced Crystallization-Driven Self-Assembly. *ACS Polym. Au* **2022**, *2* (6), 501−509.
(25) Farmer, M. A.; Musa, O. M.; Armes, S. P. Combining Crystallization-Driven Self-Assembly with Reverse Sequence Polymerization-Induced Self-Assembly Enables the Efficient Synthesis of Hydrolytically Degradable Anisotropic Block Copolymer Nano-Objects Directly in Concentrated Aqueous Media. *J. Am. Chem. Soc.* **2024**, *146* (24), 16926−16934.
(26) Zhang, X.; Chen, G.; Liu, L.; Zhu, L.; Tong, Z. Precise Control of Two-Dimensional Platelet Micelles from Biodegradable Poly(*p*-dioxanone) Block Copolymers by Crystallization-Driven Self-Assembly. *Macromolecules* **2022**, *55* (18), 8250−8261.
(27) Su, Y.; Jiang, Y.; Liu, L.; Xie, Y.; Chen, S.; Wang, Y.; O'Reilly, R. K.; Tong, Z. Hydrogen-Bond-Regulated Platelet Micelles by Crystallization-Driven Self-Assembly and Templated Growth for Poly(ε-Caprolactone) Block Copolymers. *Macromolecules* **2022**, *55* (3), 1067−1076.
(28) Xiao, L.; Parkinson, S. J.; Xia, T.; Edge, P.; O'Reilly, R. K. Enhancing the Scalability of Crystallization-Driven Self-Assembly using Flow Reactors. *ACS Macro Lett.* **2023**, *12* (12), 1636−1641.
(29) Xia, T.; Xiao, L.; Sun, K.; Rho, J. Y.; Xie, Y.; Parkinson, S. J.; Sangroniz, L.; Zhang, J.; Lin, J.; Müller, A. J.; et al. Control over Aspect Ratio and Polymer Spatial Distribution of 2D Platelets via Living Crystallization-Driven Self-Assembly. *Macromolecules* **2024**, *57* (23), 11210−11220.
(30) Gao, Z.; Zhang, X.; Zheng, B.; Gu, J.; Tong, Z. Creation of Segmented Platelets with Diverse Crystalline Cores Using Double Crystalline Triblock Copolymers. *J. Am. Chem. Soc.* **2025**, *147* (6), 5172−5181.
(31) Yang, S.; Kang, S.-Y.; Choi, T.-L. Morphologically Tunable Square and Rectangular Nanosheets of a Simple Conjugated Homopolymer by Changing Solvents. *J. Am. Chem. Soc.* **2019**, *141* (48), 19138−19143.
(32) Cha, Y.; Jarrett-Wilkins, C.; Rahman, M. A.; Zhu, T.; Sha, Y.; Manners, I.; Tang, C. Crystallization-Driven Self-Assembly of Metallo-Polyelectrolyte Block Copolymers with a Polycaprolactone Core-Forming Segment. *ACS Macro Lett.* **2019**, *8* (7), 835−840.
(33) Pearce, S.; He, X.; Hsiao, M.-S.; Harniman, R. L.; MacFarlane, L. R.; Manners, I. Uniform, High-Aspect-Ratio, and Patchy 2D Platelets by Living Crystallization-Driven Self-Assembly of Crystallizable Poly(ferrocenyldimethylsilane)-Based Homopolymers with Hydrophilic Charged Termini. *Macromolecules* **2019**, *52* (16), 6068−6079.
(34) Yang, S.; Kang, S.-Y.; Choi, T.-L. Semi-Conducting 2D Rectangles with Tunable Length via Uniaxial Living Crystallization-Driven Self-Assembly of Homopolymer. *Nat. Commun.* **2021**, *12* (1), 2602.
(35) Park, S.; Kang, S.-Y.; Yang, S.; Choi, T.-L. Independent Control of the Width and Length of Semiconducting 2D Nanorectangles via Accelerated Living Crystallization-Driven Self-Assembly. *J. Am. Chem. Soc.* **2024**, *146* (28), 19369−19376.
(36) Fan, B.; Wang, R.-Y.; Wang, X.-Y.; Xu, J.-T.; Du, B.-Y.; Fan, Z.-Q. Crystallization-Driven Co-Assembly of Micrometric Polymer Hybrid Single Crystals and Nanometric Crystalline Micelles. *Macromolecules* **2017**, *50* (5), 2006−2015.
(37) Huang, F.; Ma, J.; Nie, J.; Xu, B.; Huang, X.; Lu, G.; Winnik, M. A.; Feng, C. A Versatile Strategy toward Donor-Acceptor Nanofibers with Tunable Length/Composition and Enhanced Photocatalytic Activity. *J. Am. Chem. Soc.* **2024**, *146* (36), 25137−25150.
(38) Tao, D.; Feng, C.; Cui, Y.; Yang, X.; Manners, I.; Winnik, M. A.; Huang, X. Monodisperse Fiber-Like Micelles of Controlled Length and Composition with an Oligo(*p*-phenylenevinylene) Core via "Living" Crystallization-Driven Self-Assembly. *J. Am. Chem. Soc.* **2017**, *139* (21), 7136−7139.

https://doi.org/10.1021/acs.macromol.5c03517
Macromolecules XXXX, XXX, XXX−XXX

(39) Schöbel, J.; Karg, M.; Rosenbach, D.; Krauss, G.; Greiner, A.; Schmalz, H. Patchy Wormlike Micelles with Tailored Functionality by Crystallization-Driven Self-Assembly: A Versatile Platform for Mesostructured Hybrid Materials. *Macromolecules* **2016**, *49* (7), 2761−2771.
(40) Hils, C.; Schmelz, J.; Drechsler, M.; Schmalz, H. Janus Micelles by Crystallization-Driven Self-Assembly of an Amphiphilic, Double-Crystalline Triblock Terpolymer. *J. Am. Chem. Soc.* **2021**, *143* (38), 15582−15586.
(41) Li, Z.; Liu, R.; Mai, B.; Wang, W.; Wu, Q.; Liang, G.; Gao, H.; Zhu, F. Temperature-Induced and Crystallization-Driven Self-Assembly of Polyethylene-*b*-Poly(ethylene oxide) in Solution. *Polymer* **2013**, *54* (6), 1663−1670.
(42) Yin, L.; Hillmyer, M. A. Disklike Micelles in Water from Polyethylene-Containing Diblock Copolymers. *Macromolecules* **2011**, *44* (8), 3021−3028.
(43) Dai, X.; Qiang, X.; Hils, C.; Schmalz, H.; Gröschel, A. H. Frustrated Microparticle Morphologies of a Semicrystalline Triblock Terpolymer in 3D Soft Confinement. *ACS Nano* **2021**, *15* (1), 1111−1120.
(44) Ding, L.; Qian, J.; Zhu, G.; Li, W.; Zhao, C.; Xu, Y.; Mu, J. Self-Assembly of Linear-Hyperbranched Hybrid Block Polymers: Crystallization-Driven or Solvent-Driven? *J. Polym. Res.* **2019**, *26* (5), 121.
(45) Shi, B.; Zhou, C.; Wang, X.; Shen, D.; Wang, G. Preparation, Characterization, and Self-Assembly of P3HT-Based Janus Fibers via a Crystallization-Driven Self-Assembly Process. *ACS Macro Lett.* **2025**, *14* (10), 1367−1374.
(46) MacFarlane, L. R.; Li, X.; Faul, C. F.; Manners, I. Efficient and Controlled Seeded Growth of Poly(3-hexylthiophene) Block Copolymer Nanofibers through Suppression of Homogeneous Nucleation. *Macromolecules* **2021**, *54* (24), 11269−11280.
(47) Qiu, H.; Gao, Y.; Du, V. A.; Harniman, R.; Winnik, M. A.; Manners, I. Branched Micelles by Living Crystallization-Driven Block Copolymer Self-Assembly under Kinetic Control. *J. Am. Chem. Soc.* **2015**, *137* (6), 2375−2385.
(48) Oliver, A. M.; Gwyther, J.; Boott, C. E.; Davis, S.; Pearce, S.; Manners, I. Scalable Fiber-like Micelles and Block Co-micelles by Polymerization-Induced Crystallization-Driven Self-Assembly. *J. Am. Chem. Soc.* **2018**, *140* (51), 18104−18114.
(49) Wang, X.; Guerin, G.; Wang, H.; Wang, Y.; Manners, I.; Winnik, M. A. Cylindrical Block Copolymer Micelles and Co-Micelles of Controlled Length and Architecture. *Science* **2007**, *317* (5838), 644−647.
(50) Li, Z. Y.; Liu, R.; Mai, B. Y.; Wang, W. J.; Wu, Q.; Liang, G. D.; Gao, H. Y.; Zhu, F. M. Temperature-Induced and Crystallization-Driven Self-Assembly of Polyethylene-Poly(ethylene oxide) in Solution. *Polymer* **2013**, *54* (6), 1663−1670.
(51) Ding, L. F.; Qian, J. Y.; Zhu, G. J.; Li, W.; Zhao, C. Z.; Xu, Y. C.; Mu, J. S. Self-Assembly of Linear-Hyperbranched Hybrid Block Polymers: Crystallization-Driven or Solvent-Driven? *J. Polym. Res.* **2019**, *26* (5), 121.
(52) Chen, W. Y.; Li, C. Y.; Zheng, J. X.; Huang, P.; Zhu, L.; Ge, Q.; Quirk, R. P.; Lotz, B.; Deng, L.; Wu, C.; et al. "Chemically Shielded" Poly(ethylene oxide) Single Crystal Growth and Construction of Channel-Wire Arrays with Chemical and Geometric Recognitions on a Submicrometer Scale. *Macromolecules* **2004**, *37* (14), 5292−5299.
(53) Hsiao, M.-S.; Chen, W. Y.; Zheng, J. X.; Van Horn, R. M.; Quirk, R. P.; Ivanov, D. A.; Thomas, E. L.; Lotz, B.; Cheng, S. Z. Poly(ethylene oxide) Crystallization within a One-Dimensional Defect-Free Confinement on the Nanoscale. *Macromolecules* **2008**, *41* (13), 4794−4801.
(54) Su, M.; Huang, H.; Ma, X.; Wang, Q.; Su, Z. Poly(2-vinylpyridine)-*block*-Poly(ε caprolactone) Single Crystals in Micellar Solution. *Macromol. Rapid Commun.* **2013**, *34* (13), 1067−1071.
(55) Keller, A. A Note on Single Crystals in Polymers-Evidence for a Folded Chain Configuration. *Philos. Mag.* **1957**, *2* (21), 1171−1175.
(56) Ungar, G.; Stejny, J.; Keller, A.; Bidd, I.; Whiting, M. C. The Crystallization of Ultralong Normal Paraffins-the Onset of Chain Folding. *Science* **1985**, *229* (4711), 386−389.
(57) He, M.; Zhang, H.; Chen, W.; Dong, X. *Polymer Physics*; Fudan University Press, 2007.
(58) Passaglia, E.; Khoury, F. Crystal Growth Kinetics and the Lateral Habits of Polyethylene Crystals. *Polymer* **1984**, *25* (5), 631−644.
(59) Organ, S.; Keller, A. Solution Crystallization of Polyethylene at High Temperatures: Part 1 Lateral Crystal Habits. *J. Mater. Sci.* **1985**, *20* (5), 1571−1585.

https://doi.org/10.1021/acs.macromol.5c03517
Macromolecules XXXX, XXX, XXX−XXX